2020

Investigating the evolution of sedimentary features near monopiles

Firth, K.

Investigating the evolution of sedimentary features near monopiles

Kate Firth

Project Advisor: Dr Jon Miles, School of Engineering, University of Plymouth, Drake Circus, Plymouth, PL4 8AA

Abstract

Many of the large windfarms off the coast of the UK are founded on sandbanks and the movement of sediment from around the monopile foundations leave the structures susceptible to severe scour pits and significant scour wake downstream. The removal of sediment not only has a negative impact on the structures but also the cables that run between each turbine. Areas of sediment accretion can cause localised overheating while areas of erosion can cause early fatigue.

The paper presents findings of laboratory experiments completed to begin to understand the propagation of the scour wake in unidirectional current flow conditions. It is found that there is much variability in the response of the sediment to current flow but there are a number of consistent trends with tests of increasing current speeds. The same experiment was completed for 6 current speeds over a mobile sediment bed. The current speeds were 0.230, 0.201, 0.187, 0.178, 0.175 and 0.149 m/s. Flow was measured using an Electromagnetic Flow Meter suspended over the sediment bed (Valeport, 2019). Each test was filmed using aerial projection and a compilation video (Firth, 2019). The footage was analysed to obtain the results of the distances travelled by the disturbance front and the individual ripples. Data collection also took place after each experiment to collect the heights of the ripples.

Trends identified in the results show that: the propagation of the ripple field front is 4 times faster than that of the individual ripples within the disturbance; the ripples migrate in 2 distinct paths and they take the form of linguoid ripples, however appear in heart shapes rather than semi-circular.

Introduction

The supply of energy from offshore wind has followed an upward trend since the early 2000's (WindEurope, 2019), with the aim it will produce over 10% of the UK's electricity by 2020 (RenewableUK, n.d.). To ensure that the positive trend continues it is vital, among other factors, that the offshore structures, producing the electricity, do not fail. Failure could occur for many reasons but due to the unpredictable nature of the sea it is likely that not all failure mechanisms may have been modelled accurately before construction. An offshore wind farm is made up of wind turbines and a network of cables. The cables have an optimal temperature for energy transfer and that temperature is dictated by many factors but the main one being the cable depth below the seabed (Sørensen and Sørensen, 2010). Unfortunately, that depth is subject to change because of the movement of sediment caused by water motion. Many windfarms in the UK are established on sand banks in the North Sea and therefore susceptible to vast sediment movement; large sand waves have been observed downstream of monopiles (Whitehouse et al, 2011).

The scour around monopiles has been researched in great detail in many papers, however there has not been further research into the effect of the scour wake and how it evolves. The build up of sediment at the peaks of the ripples creates greater distances between the top of the cable and the exit for heat at the seabed. This increase in sediment depth above the cable can lead to the cables overheating and experiencing from localised failure. Additionally, areas of scour at the trough of the ripples can result in free hanging sections of cables which could be susceptible to fatigue. According to Thies, Johanning and Smith (2012) there are 3 mechanical failure modes of cables connected to offshore energy converters. Although the cables at monopiles will not be susceptible to all 3 failure modes, as they are static, they will be susceptible to the third which is degradation failure under extreme dynamic and cyclic loads (Thies, Johanning and Smith, 2012) if the cables become exposed to the actions of the wave and current. As the cables are designed to be buried it is unlikely they will be able to withstand the extreme dynamic conditions they will become exposed to if they become free hanging.

This study aims to concentrate on how the scour wake propagates downstream to create ripples in the seabed. It aims to realise a rate of migration and angle of propagation by physical modelling, with ripple wavelengths and depths measured to begin to quantify the impact that ripples may have on the functionality of the offshore windfarms.

Literature Review

There is currently no literature that researches the scour wake produced downstream of a monopile and how it propagates but scour, in general, has been researched thoroughly by Zanke (1982), Whitehouse (1998) and Sumer (1992) among others. The review of literature will, therefore, consider research undertaken to understand scour, and also monopiles and seabed formation. The report is the culmination of these 3 elements so it sees fit to review literature based on these, due to the lack of literature on the specific topic.

Scour

Scour is the "localised movement of sediment" (Carter, 2007) that occurs rapidly at structures then asymptotically to equilibrium (Whitehouse, 1998) when the critical condition for sediment transport is exceeded by the ambient current at the structure (Zanke et al., 2011). Zanke et al (2011) found the primary influences on scour were the Keulegan-Carpenter number (KC) and the relationship between the critical velocity for sediment movement and flow velocity, u/u_c. The Keulegan-Carpenter number is a dimensionless quantity that describes flow excursion relative to pile diameter (Miles, 2018).

$$KC = \frac{uT}{D}$$

Where u is the flow velocity, T is the period of oscillation and D is the diameter of the monopile (Miles, 2018). It suggests that a large KC value is given by water moving considerably in relation to the pile diameter and therefore causing substantial scour. The larger the KC number, the greater the scour. Sumer et al (1992) state that "the scour increases with increasing KC number" when KC>6. Zanke (1982) developed a solution for scour depth occurring in steady flow:

$$\left(\frac{H}{D}\right) steady\ flow \approx 2.5 \left(1 - 0.5\frac{u_c}{u}\right)$$

Where, H is the equilibrium scour depth, D is the pile diameter, u_c is the critical velocity for beginning of sediment motion and u is the maximum near bed velocity of wave induced orbital currents namely mean velocity in the case of steady currents (Zanke et al journal (2011)).

Scour is induced by the turbulent vortices formed by flow being deflected downwards to the seabed when approaching the obstacle (CIRIA, 2015) and then rolling up to create a recirculating eddy (primary vortex) which wraps around the pile and then begins to travel downstream (Whitehouse, 1998) disrupting the surface of the sediment to cause the scour pit. Beyond the scour pit the seabed is affected by the flow being disrupted by the disturbances to the sediment that have occurred upstream, which in turn creates the next disturbance (Whitehouse, 1998). CIRIA (2015) suggest that the horseshoe vortices become wake vortices beyond the pile and in turn produce twin longitudinal scour holes which are likely to affect the next structure downstream if located within the wake.

Scour pits

Scour pits, often referred to as scour holes, are the areas of erosion directly adjacent and surrounding a marine structure caused by the removal of sediment due to the flow of water above it. The flow is stronger than the shear strength of the sediment and moves it in a process of saltation (Masselink and Hughes, 2003); it is placed in an area of accretion. Accretion is build-up of sediment to create an area of growth.

Scour wake

Scour wake is the term for scour occurring downstream of the structure to form a ripple effect in the bedform. The ripples are the combination of areas of erosion and

accretion created by the flow separating around the pile. Sand waves have been observed downstream of monopiles by Whitehouse et al (2011).

Clear-water Scour

Clear-water scour is the term denoted to the conditions when the ambient bed shear stress, τ_0, is less than the critical value for sediment motion, τ_{cr}, but greater than τ_{cr}/M, where M is the shear stress amplification factor adjacent to the structure (Whitehouse, 1998). This suggests the threshold velocity is only exceeded due to flow acceleration around the pile. Once the flow has increased enough to allow a supply of sediment from upstream then this has become live-bed scour (CIRIA, 2015). If the flow then reduces it may return to clear-water scour conditions.

Scour depth encouraged by clear-water scour is greater than that of live-bed scour, attributed to the eroded areas not being built up by sediment travelling from upstream during clear-water scour conditions (CIRIA, 2015).

Monopiles

Monopiles are cylindrical steel tubes commonly used as foundations in offshore windfarms, however they are limited by the deflection and vibration they are subjected to (4c offshore, 2013). Typically, monopiles have a diameter up to 6m, weigh up to 650 tonnes and can be used in water depths between 0 and 30m (4Coffshore, 2013).

An additional problem faced by monopiles is the damage to their structural stability and integrity when sediment is removed from around them in the scouring process (Whitehouse et al, 2011). Scour reduces the lateral capacity of the monopiles due to removing the support around the structure, in turn changing the structural stiffness and natural frequency of the piles which could increase fatigue stress in the structure and operational issues (Li et al., 2018).

Scour protection at Monopiles

Often scour protection is placed retrospectively when the scour pit has reached its equilibrium depth (CIRIA, 2007). It is placed to fill the scour pit to avoid more damage to the structural stability of the monopile (Whitehouse et al, 2011).

With scour protection

Despite the benefit of placing scour protection to the structural integrity of the structure, there is a possibility that the protection may induce secondary scour (CIRIA, 2007). Secondary scour is the removal of sediment from the edge of the primary scour protection; with potential to cause the failure of the scour protection and in turn the exposure of the structure and cables. The response of this scour is likely, however, to be much less significant than if the protection was not present (CIRIA, 2007). Whitehouse et al's (2011) fieldwork at Scroby sands suggests that the protection may influence additional scour to occur. Retrospective protection was put in place at Scroby Sands once and the depth variation is much greater in November 2006 than February 2004, suggesting secondary scour has occurred.

Seabed formation

Masselink and Hughes (2003) state there are a number of classifications for bedform distinguished by dimension and depending on if flow is unidirectional or oscillatory. These bedforms can take a variety of shapes.

Although ripples and dunes can be determined by their size, there are behavioural characteristics that can also make them distinguishable (Masselink and Hughes, 2003) such as dependence on flow velocity or water depth; ripples and dunes both increase in size with increasing flow velocity, but dune size is also determined by water depth.

The experiment to follow in this paper will be based on unidirectional current only so the review will continue with relevant current literature; unidirectional flow can cause either ripples or dunes in the bedform.

Ripples

Reeve, Chadwick and Fleming (2018) state that ripples, generated by current, will form for sediment diameters of up to 0.8mm. Wavelength (λ_r) and wave height (H_r) of sand ripples in unidirectional flow can be estimated by $\lambda_r = 1000D_{50}$ and $H_r = \lambda_r/7$, with typical measured values of $\lambda_r = 0.14$m and $H_r = 0.016$m (Reeve, Chadwick and Fleming, 2018).

Leeder (1982) corroborates $\lambda_r = 1000D_{50}$ (Reeve, Chadwick and Fleming, 2018) and that current ripples do not occur in sands of diameter greater than 0.7mm. They are formed of a gentle slope on the upstream side and steep slope downstream (Leeder, 1982). Leeder (1982) and Pye (1994) suggest sediment is moved up the shallow side of the ripple until it settles at the top of the slope to create the steep downstream face; the steep side can become unstable and cause sediment avalanches that settle at the bottom of the steep slope. This settlement causes turbulence in the flow (Leeder, 1982). The turbulence causes the sediment to shift to form the next shallow upstream slope, causing the ripples to propagate downstream (Pye, 1994).

Leeder (1982) suggests the increase in size of the ripples is independent of the depth of the water but highly dependent on the bed shear stress.

Theory of Self-organisation

According to $\lambda_r = 1000D_{50}$ (Reeve, Chadwick and Fleming, 2018; Leeder, 1982) the wavelength of each individual ripple is only dependent on the diameter of the sediment, however there is a theory of self-organisation (Gallagher, 2011) which suggests that the wavelength will increase in a logarithmic manner forever if the conditions do not change. The theory decouples the wavelength and height from the grain size and velocity but dictates that as long as the sediment is being moved by the flow then realistic bed formations will develop in a self-organised manner (Gallagher, 2011).

There are many morphological patterns that have been suggested to be self-organised (Gallagher, 2011) where patterns are born from the non-linear interactions of the affected area and its environment (Gallagher, 2011). These environments are all open so material and energy is transported across area boundaries by dissipative processes (Werner, 1999) where the focus for ripples is on sediment transport. Masselink (2019) discussed a sediment "box" that the sediment is moved within but does not leave so all accretion and erosion occurs within the "box", however the open environments suggested by Werner (1999) allow the sediment to travel across these "box" boundaries.

Summary

Large amounts of research has been completed to contribute to understanding the development of scour pits around monopiles. The following report will provide experimental data from a laboratory experiment to understand the development of scour wake, downstream of the monopiles, and compare results to existing research. It will provide information to make efforts to fill the knowledge gap in the industry to increase understanding of scour as a whole.

Methodology

Primary research took place on the Alborn rig in the Marine Building, University of Plymouth.

Apparatus

Figure 1 shows a sketch of the cross section of the Alborn rig with internal details shown in the form of a dashed line. The rig consists of: a mobile sediment bed, a paddle to adjust the water depth and a pump to ensure constant flow over the sediment. The experiment was filmed using aerial projection of a mobile phone above the rig. Light was provided by an LED panel on the side of the tank; the overhead lights were covered to reduce the impact of the shadows they produced.
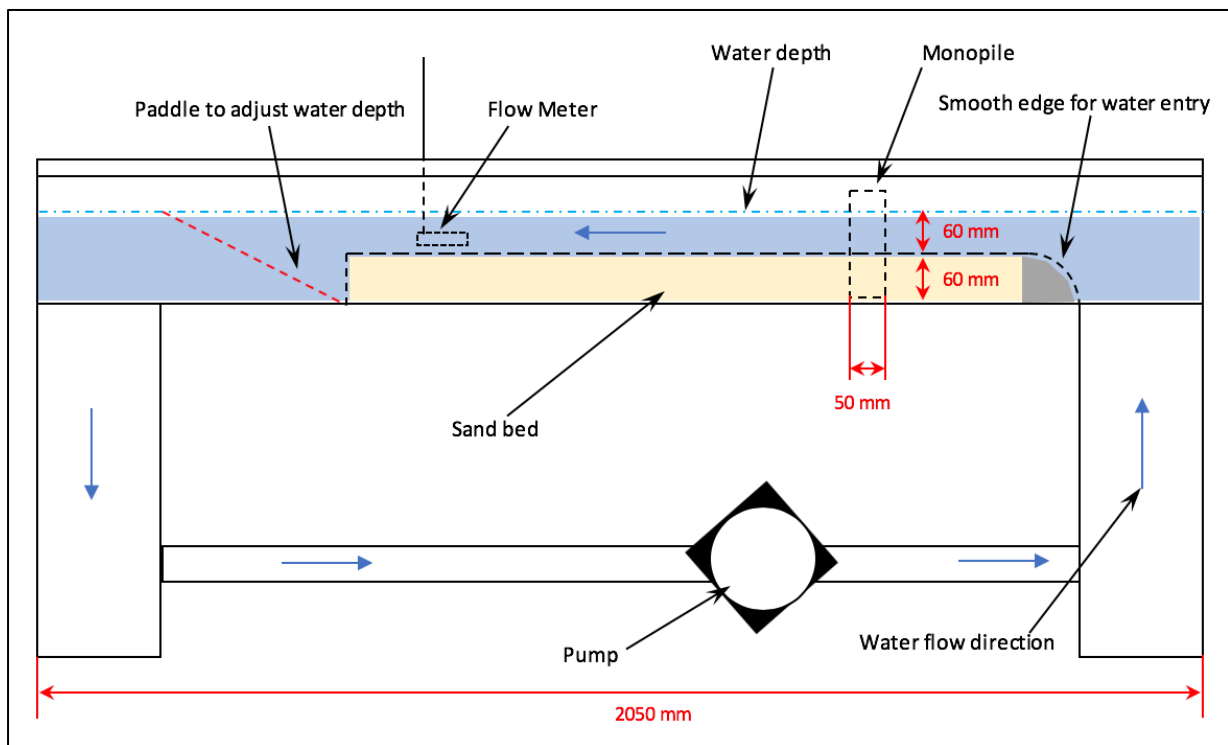

Figure 1: Sketch of cross-section of Alborn Rig

The current velocity was measured using a Model 801 (flat) Valeport EM Flow Meter. The unidirectional flow was controlled by a valve next to the pump. Distance measurements were all taken in relation to a tape suspended over the rig.

Scaling
The factors determining the scale of the experiment were the dimensions of the Alborn rig; water depth being the leading dimension. The maximum water depth that can be achieved in the working area of the rig is 60mm over the sand bed, therefore all other dimensions were dictated by this. The experiment used an undistorted scale.

Table 1: Scaled Dimensions

	Model	Prototype
Water Depth	60 mm	6000 mm
Sand Depth	60 mm	6000 mm
Pile Diameter	50 mm	5000 m
Wall Thickness	4 mm	400 mm
Rig Width	600 mm	60000 mm
Rig Length	2050 mm	205000 mm

A scale factor of 100 was used to achieve the comparison between model and prototype dimensions. Froude scaling was used for current velocity.

$$\frac{V_P}{V_M} = \sqrt{Scale\ Factor}$$

Where, V_P and V_M are the current velocities of the prototype and model, respectively.

Assuming $V_P \cong$ 2.5 m/s, for example, then V_M = 0.25 m/s. The tested velocities were dictated by the capability of the rig and there had to be compromise between the water depth and the current velocities. The current speed could be increased with a shallower water depth therefore balance had to be met between the two variables. The depth had to be great enough to be realistic however, the velocity had to be great enough to ensure sediment transport occurred.

Froude scaling was chosen over Reynolds scaling as Reynolds scaling assumes that the viscosity of the fluid must be scaled, however this is a requirement that cannot be met. Water was used in the model, therefore the Reynolds number is not preserved, however in both lab and field situations the flow is turbulent.

Additionally, the sediment was not scaled therefore creating a scale effect in the model, however, if a finer sediment had been used then the sand would have acted in a cohesive fashion and therefore not have yielded accurate results. Sand with D_{50} $\cong$ 0.2 mm was used. Petersen et al (2015) used a grain size of 0.17mm, therefore by using 0.2mm fine non-cohesive sand follows the same approach. As air entrapment cannot be scaled, it was critical that there was enough water to flow around the tank to ensure the pump did not begin to emit air into the experiment and disturb the sediment.

Calibration

To ensure the flow meter was measuring the current velocities accurately, a calibration was completed to compare the flow meter results with a polystyrene float test.
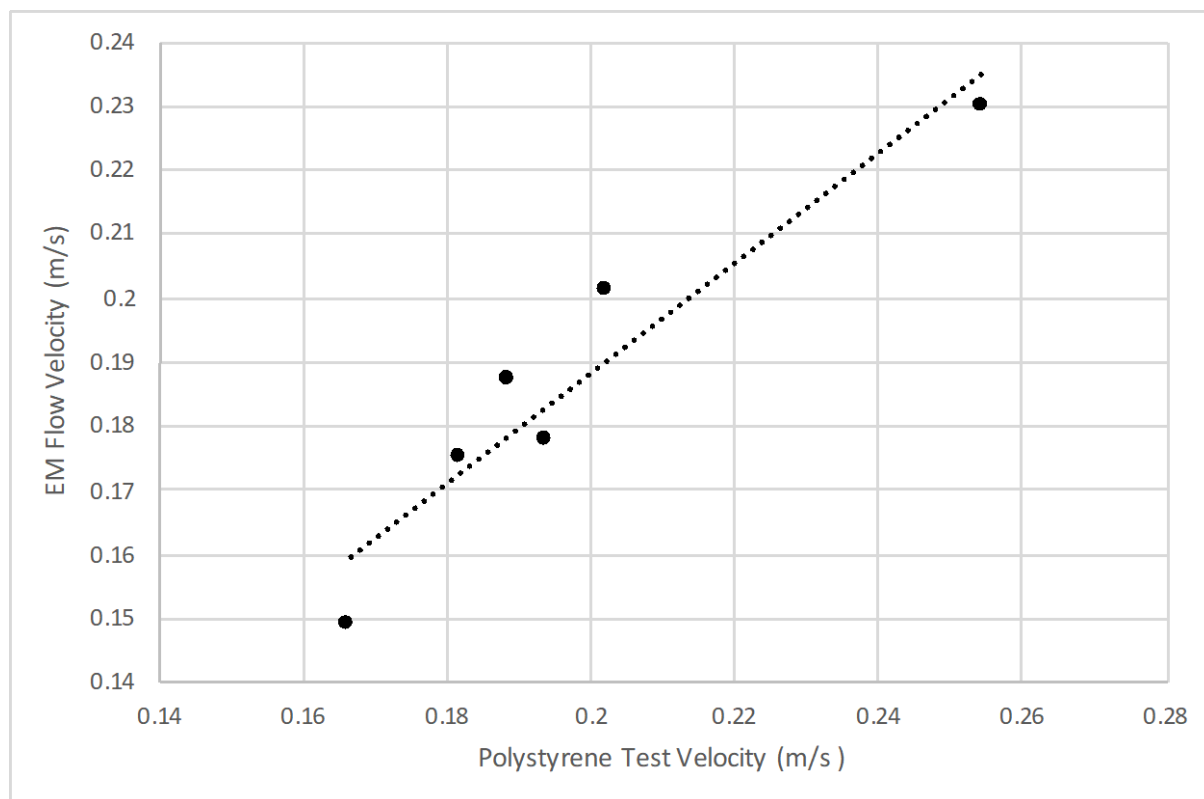

Figure 2: Graph to show the calibration of the flow meter readings and polystyrene tests. The polystyrene data is presented on the x axis and the EM Flow data is presented on the y axis. A linear trendline has been plotted to allow comparison of the data.

Figure 2 shows the flow meter values are very close to those recorded during the polystyrene tests; approximately 0.005 m/s different. The polystyrene tests were completed by timing how long it took the polystyrene to cover a determined distance by floating on the surface of the water; human error due to reaction speed could account for the small difference in recordings.

To increase the accuracy of each measurement taken from the flow meter, 60 second averages were used; minimising the effect of "noisy real time recordings" (Valeport, 2019).

Procedure

Experiment

The experiment followed the same procedure for 6 current speeds with 2 of the tests having very similar current speeds to begin to understand if the tests were repeatable.

Table 2: The currents speeds measured by the flow meter for each test.

Test	Current Speed (m/s)
1	0.230
2	0.201
3	0.187
4	0.175
5	0.149
6	0.178

The setup of the individual tests was completed by saturating the sand and smoothing it using the plasterer's float to ensure the testing bed was flat. This allowed each test to begin with the same conditions to ensure comparisons could be made and trends distinguished from the results. It had to be ensured that the sand was level with the entrance ramp so there was no unnatural turbulence created before the flow reached the pile.

Figure 3: Setup of the sediment bed using a plasterer's float

The measuring tape was moved in-line with the flow meter, at the centre of the rig, and as close to the water level as possible, without disturbing the flow, to avoid parallax errors when taking measurements. Parallax errors would be produced by the camera, without avoidance, therefore it was required to minimise those that could be managed. The position of the flow meter was constant in every test and placed far downstream, so it did not affect the results; it could have caused disturbance to the flow of the water and induce scour of its own, making the experiment misrepresentative of reality.

Figure 4: Flow meter suspended over the sediment bed.

The steel model monopile was embedded in the sediment until it reached the base of the sediment bed and placed in approximately the same location for every test, in one motion to minimise the unnatural disturbance to the sediment. The diameter of the pile was 50 mm to represent a prototype pile diameter of 5 m.

Figure 5: Alborn rig setup with LED panel light, suspended tape, flow meter and steel model monopile in place.

Aerial projection recording allowed for each test to be filmed. A time stamp was used to keep time of the experiment and assess the progress that was being made. The unidirectional flow was turned on and once full water depth had been established, the flow meter readings were taken. Water depth was recorded for each test and the flow checked periodically. It was essential to periodically check that the

camera was still recording the tests. Unfortunately, 1 test had to be re-run as the camera reached its storage capacity and stopped recording after roughly 10 minutes.

Each test was run until the ripples had surpassed the edge of the sediment bed. The flow was stopped, camera turned off and depth and distance measurements were taken. The process was repeated for all chosen current speeds. The final test had a current speed 0.003 m/s faster than one of the previous tests to begin to determine if the results were repeatable or random each time. Observations from the initial tests suggested that the response would not be exactly the same but may present a very similar ripple field of depths and wavelengths.

Sieve Gradation

Once all tests were completed, a sand sample was removed from the rig and oven-dried overnight to be sieved to determine the gradation of the sand. Table 3 provides the results of the sieving and hence determines that the sand had $D_{50} \cong 0.2$ mm. Figure 6, Figure 7 and Figure 8 depict stages of the sieving process.

Table 3: Sieve gradation of the sand sample from the Alborn rig. Column 1 shows the gradation of the 10 sieves that were used and columns 2 to 4 present the weights of the sand, sieve and total mass to obtain the gradation. The cells that are highlighted green show the cumulative weights beyond 50% of the sample to determine d_{50}.

Size (mm)	Weight (g)			
Nominal Opening Size	Total	Sieve	Sand	Cumulative Sand
1	340.6	339.5	1.1	1.1
0.9	485	484.5	0.5	1.6
0.8	442.9	442.3	0.6	2.2
0.71	466.9	466.3	0.6	2.8
0.6	444.3	443.4	0.9	3.7
0.5	385.9	384.8	1.1	4.8
0.4	403.3	397.6	5.7	10.5
0.315	412.6	386.2	26.4	36.9
0.25	423.3	354.1	69.2	106.1
0.2	537.9	386.2	151.7	257.8
0.16	323.6	273.7	49.9	307.7
0.125	360.4	346	14.4	322.1
0.063	331.8	328.2	3.6	325.7
Pan	250.5	250.3	0.2	325.9

Figure 6: Sieve stack for gradation – 10 sieves with decreasing mesh sizes

Figure 7: Shaker used to ensure sample separated entirely into the correct sieves

Figure 8: Each sieve was weighed with its contents and the known weights of the sieves were then taken away to determine

Data Collection
Data was collected by videoing each test with a mobile phone above the rig. This allowed data analysis to be completed once all of the tests had been finished to allow for comparison of the results. Distance measurements were taken relative to the tape suspended over the rig and the depth measurements were taken using a vertical sand level gauge, as seen in Figure 9 and Figure 10. The timestamp on the video recordings was used in the analysis.

Figure 6: Using the shadows produced by the vertical sand level gauge to ensure the measurement is being taken on the surface of the sediment

Figure 7: Reading the depth measurement

The current measurements were recorded on a spreadsheet throughout the testing, along with any observations that were made during the experimental process. Polystyrene tests were completed to continue the assurance that the flow meter was calibrated and producing accurate results.

Data Analysis
Using the aerial footage, migration rates were established for the ripple field and a chosen individual ripple from each test.

Migration of ripple field front
There were 2 methods used to determine the migration rate of the leading edge of the ripple field. It was ensured that a time was chosen where a whole ripple had been formed to clearly identify the end of the ripple. Distances were measured according to the tape measure suspended over the water. There were 2 sides to the wake and the same side of the ripple field was analysed each time for consistency.

The first method consisted of taking the overall distance the ripple field front had travelled until it was no longer in the view of the camera and dividing it by the length of time it took to reach this distance. These migration rates were then used to compare the distances travelled for each current speed with a chosen length of time. By manipulating the data in this way, all of the tests could be compared, despite the data being recorded for different durations and yielding different length ripple fields;

no constants. This produced an average migration rate and did not consider any changes in the migration rate through time. Table 4 provides the raw data from the videos and converts it using this method.

Table 4: Whole Field - Rate of Migration to obtain the average migration rate until the ripple front had travelled beyond the filmed area.

Test	Current (m/s)	Start Time	End Time	Time	Time (s)	Upstream position	Downstream position	Distance (mm)	Distance (m)	Rate (mm/s)	Rate (m/s)
1	0.23	09:58:53	10:52:01	00:53:08	3188	950	89	861	0.861	0.270	2.70E-04
2	0.201	14:05:28	15:14:05	01:08:37	4117	1045	109	936	0.936	0.227	2.27E-04
3	0.187	12:05:44	12:45:46	00:40:02	2402	1045	92	953	0.953	0.397	3.97E-04
4	0.175	14:58:21	15:55:08	00:56:47	3407	1050	135	915	0.915	0.269	2.69E-04
5	0.149	09:58:36	11:22:47	01:24:11	5051	1042	120	922	0.922	0.183	1.83E-04
6	0.178	14:12:34	15:01:59	00:49:25	2965	1055	145	910	0.910	0.307	3.07E-04

Figure 11 shows a screenshot of the footage from Test 2 with the marked red lines showing the length of propagation of the ripple field. All field length measurements were determined from the upstream edge of the scour pit, allowing for the whole affected area to be measured, including the scour pit.

Figure 8: Screenshot of footage from Test 2

Assuming the migration rate is constant forever then, Table 5 uses of the rates of migration, from Table 4, to standardise the lengths of time and provide a projected distance the whole field will have travelled in the model and prototype, for Test 1.

Table 5: Manipulation of the whole field data, for Test 1, dictated by the rates of migration found in Table 5

	Model	Model		Model & Prototype		Model		Prototype			
Test	Current (m/s)	Time (hh:mm:ss)	Time (s)	Rate (mm/s)	Rate (m/s)	Distance (mm)	Distance (m)	Distance (m)	Time (s)	Time (dd:hh:mm:ss)	Current (m/s)
1	0.23	01:00:00	3600	0.270	2.70E-04	972.27	0.97	97.23	36000	00:10:00:00	2.3
		02:00:00	7200	0.270	2.70E-04	1944.54	1.94	194.45	72000	00:20:00:00	2.3
		03:00:00	10800	0.270	2.70E-04	2916.81	2.92	291.68	108000	01:06:00:00	2.3
		04:00:00	14400	0.270	2.70E-04	3889.08	3.89	388.91	144000	01:16:00:00	2.3
		05:00:00	18000	0.270	2.70E-04	4861.36	4.86	486.14	180000	02:02:00:00	2.3

The second method of analysis consisted of determining the distance that the overall ripple front had travelled in each 15 minute period of the test, allowing for variation in the migration rate over the length of the test. Table 6 presents the method for the data obtained from video of Test 1 (0.230 m/s).

Table 6: Whole Field - Rate of Migration to obtain the migration rate for each 15 minute period until the ripple front had travelled beyond the filmed area.

Test	Current (m/s)	Start Time	End Time	Cumulative Time (s)	Upstream position	Downstream position	Distance (mm)	Distance (m)	Rate (mm/s)	Rate (m/s)
1	0.23	09:58:53	09:58:53	0	-	-	0	0	-	-
		09:58:53	10:13:53	900	936	650	286	0.286	0.318	3.18E-04
		10:13:53	10:28:53	1800	650	550	100	0.100	0.111	1.11E-04
		10:28:53	10:43:53	2700	550	400	150	0.150	0.167	1.67E-04
		10:43:53	10:52:01	3188	400	89	311	0.311	0.637	6.37E-04

There is significant variation in the migration rates in each 15 minute period, suggesting the rates obtained in Table 4 would not represent the whole experiment. The rate of migration seems to slow down as more time passes then increases rapidly.

Migration of individual ripples
There was only one method used for tracking the individual ripple speed. One ripple was tracked from each test to allow for analysis of the propagation of the individual ripple fronts. The front of the ripple was tracked by moving forward and backwards through the video to determine when that ripple began and when it ended. It was tracked until a new ripple was formed within it so was no longer propagating as a single ripple front. Figure 12 shows a series of screenshots of the individual ripple front being tracked down the rig.
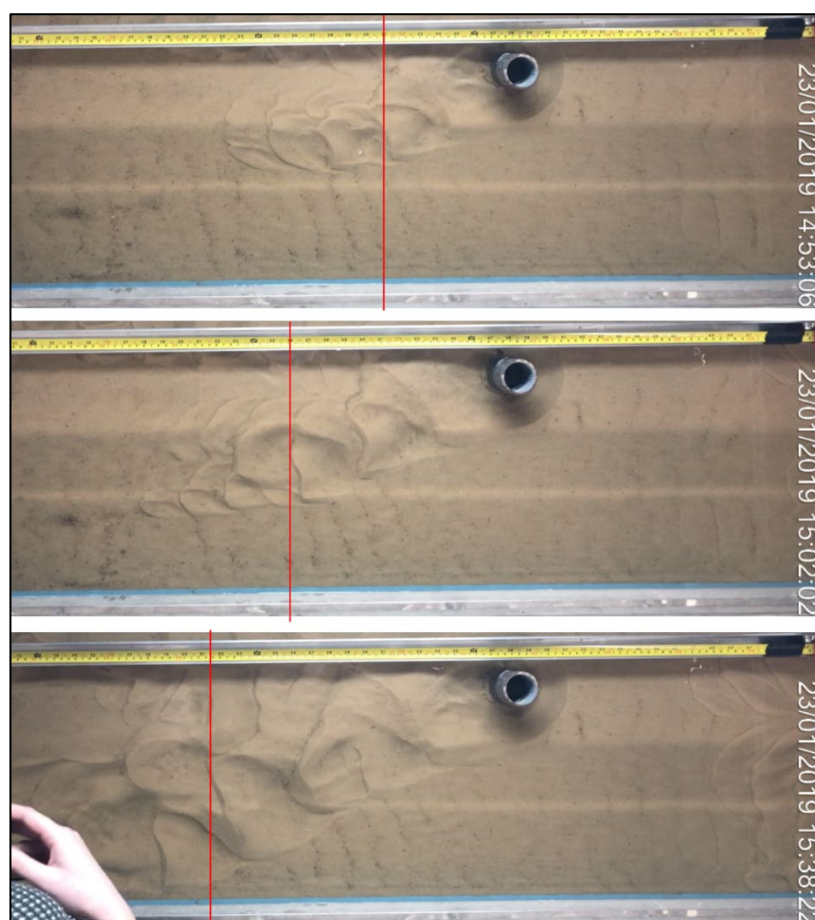

Figure 9: Series of screenshots to show how an individual ripple was tracked to obtain its migration rate. The red lines dictate the most downstream point of the individual ripple fronts.

Although the whole individual ripple front had not propagated by the same distance, due to the shape of the ripples, this is the beginning of the next ripple so it was decided that this would be the point to track each observation.

Table 7 presents the migration rate of the individual chosen ripple from each test.

Table 7: Individual Ripple - Rate of Migration

Test	Current (m/s)	Start Time	End Time	Time	Time (s)	Upstream position	Downstream position	Distance (mm)	Distance (m)	Rate (mm/s)	Rate (m/s)
1	0.23	10:36:45	11:35:31	00:58:46	3526	620	475	145	0.15	0.041	4.11E-05
2	0.201	14:53:06	15:38:22	00:45:16	2716	711	545	166	0.17	0.061	6.11E-05
3	0.187	12:31:25	12:59:33	00:28:08	1688	711	585	126	0.13	0.075	7.46E-05
4	0.175	15:57:40	16:30:31	00:32:51	1971	625	480	145	0.15	0.074	7.36E-05
5	0.149	10:40:17	11:29:49	00:49:32	2972	720	570	150	0.15	0.1050	5.05E-05
Rep.	0.178	14:26:56	15:17:57	00:51:01	3061	787	645	142	0.14	0.046	4.64E-05

Visual Analysis
The images in Figure 13 are taken from the aerial footage. All of the footage was put together in a compilation video to allow for visual comparison of the migration rates. The footage could then be used to corroborate the results that have been plotted.
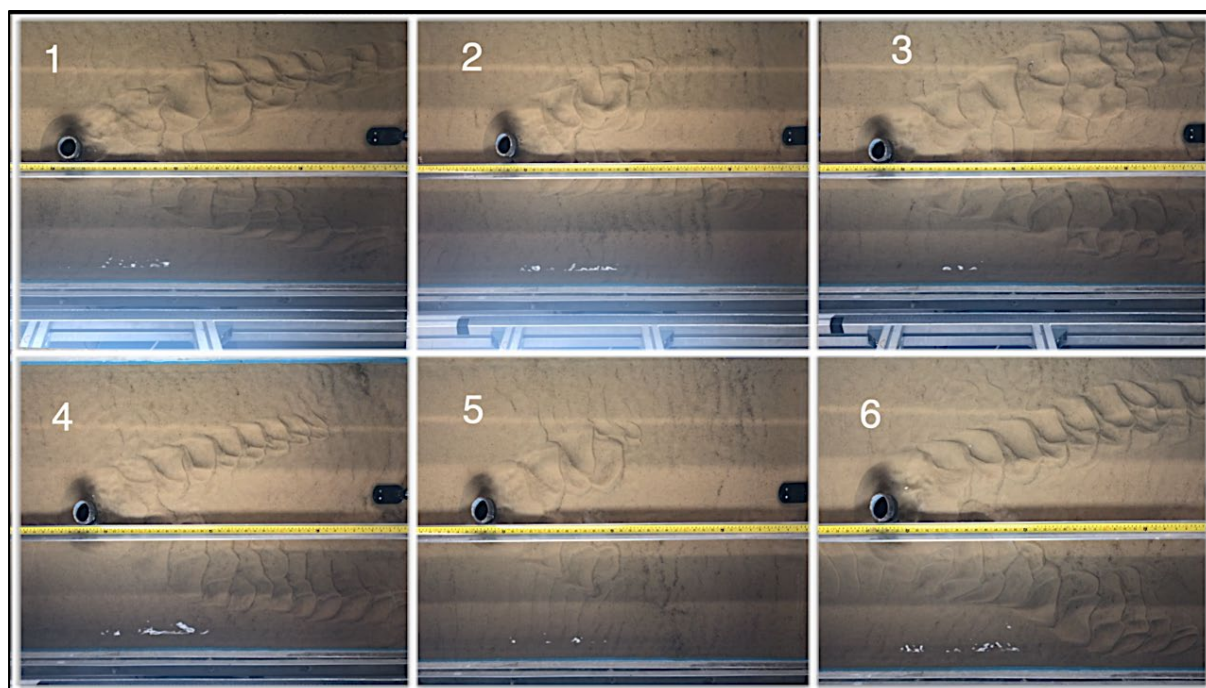

Figure 10: Screenshot of the compilation video showing the visual results of all 6 tests from the aerial camera. The screenshot is taken while all of the tests were in progress.

All 6 tests produced very similar visual results with the ripples forming in 2 distinct lines propagating at an acute angle from the edge of the scour pit.
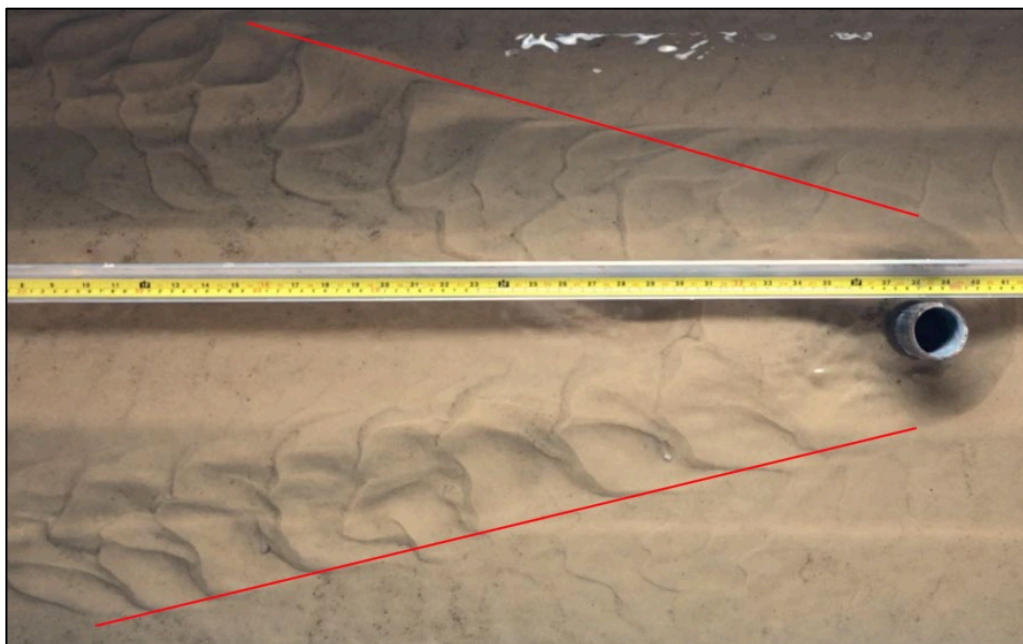
Figure 11: 2 distinct ripple fronts are produced by the monopile at each current velocity

Figure 14 shows the 2 distinct lines of ripples that have propagated down the tank in each test, showing that the disturbance does not occur directly downstream from the pile but instead at an angle. The angle of propagation also seems to reduce as the ripple travels further downstream, however this may be due to the influence of the sides of the rig.

As the individual ripples propagate downstream they portray linguoid ripples, however are not semi-circular. Each ripple has a similar heart shape; narrower upstream than downstream.
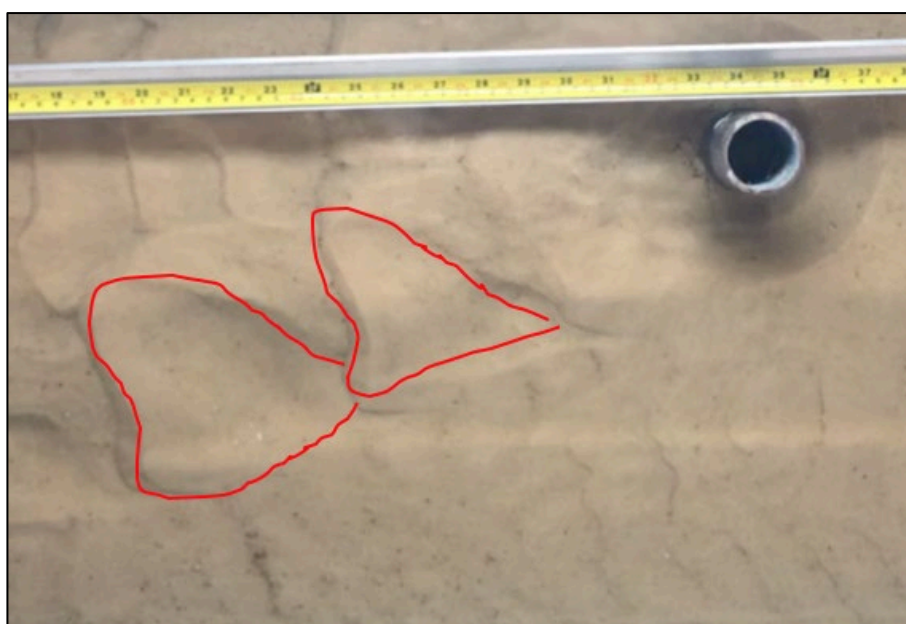
Figure 12: Sketch of the ripple shape

The ripples continue to progress downstream, despite the scour hole no longer developing, suggesting it has reached equilibrium. The ripples do not seem to reach any equilibrium, in the filmed length of time, they propagate indefinitely, and only seem to be limited by the height of the disturbance. It is assumed that once the ripple height has reached zero then the front will no longer propagate. This is observed directly downstream of the pile as the disturbance quickly reaches zero and does not propagate further.

Results

Migration of the leading edge of the Ripple Field

Graphs have been produced to begin to identify trends within the data by plotting distance against time to give migration rate, and distance and migration rate against current.
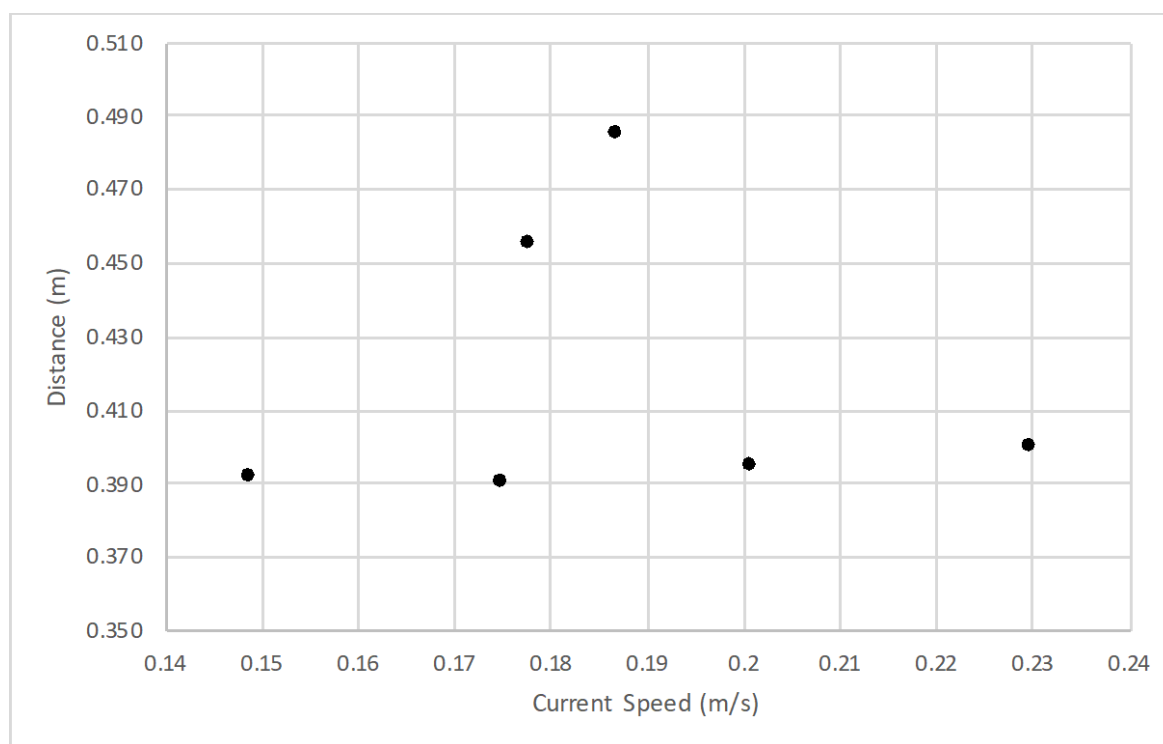
Figure 13: Graph of distance against current for a test period of ½ an hour, for all 6 tests.

There is not an obvious trend established from the data recorded in the experiments as there is considerable spread in Figure 16, suggesting that the migration rate may not increase uniformly with current velocity.
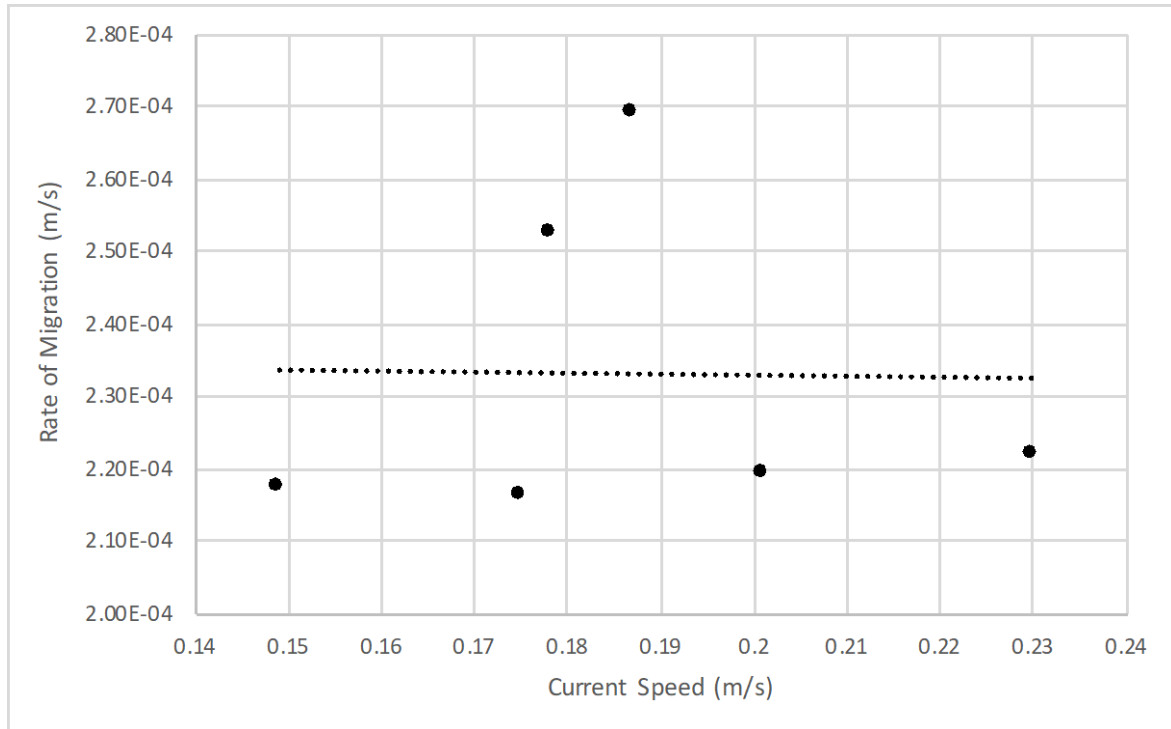
Figure 14: Graph of migration rate against current for a test period of ½ an hour, for all 6 tests

Similarly to Figure 16, Figure 17 does not present an obvious trend, suggesting that the propagation speed is independent of the current velocity once the threshold velocity has been reached. Threshold velocity, $\bar{U}_{cr}$, can be calculated using Soulsby's (1997) equation which considers sediment diameter, density of the water and the sediment and the kinematic viscosity of the water.

$$\bar{U}_{cr} = 7 \left(\frac{h}{d_{50}}\right)^{\frac{1}{7}} [g(s-1)d_{50}f(D_*)]^{\frac{1}{2}}$$

For $D_* > 0.1$
Where,

$$f(D_*) = \frac{0.30}{1 + 1.2D_*} + 0.055[1 - \exp(-0.020D_*)]$$

$$D_* = \left[\frac{g(s-1)}{v^2}\right]^{\frac{1}{3}} d_{50}$$

s = ratio of densities of grain and water
v = kinematic viscosity of water

Using,

d_{50} = 0.2 mm
ρ_s = 1650 kgm⁻³
ρ_w = 1000 kgm⁻³

ν = 1.004 x 10^{-6} m^{2}s^{-1}

Then,

$\bar{U}_{cr}$ = 0.1295 ms^{-1}

All tested current speeds were greater than the threshold velocity and therefore sediment transport occurred. Figure 17 suggests that the average migration rate of the ripples is roughly 0.00023 m/s.
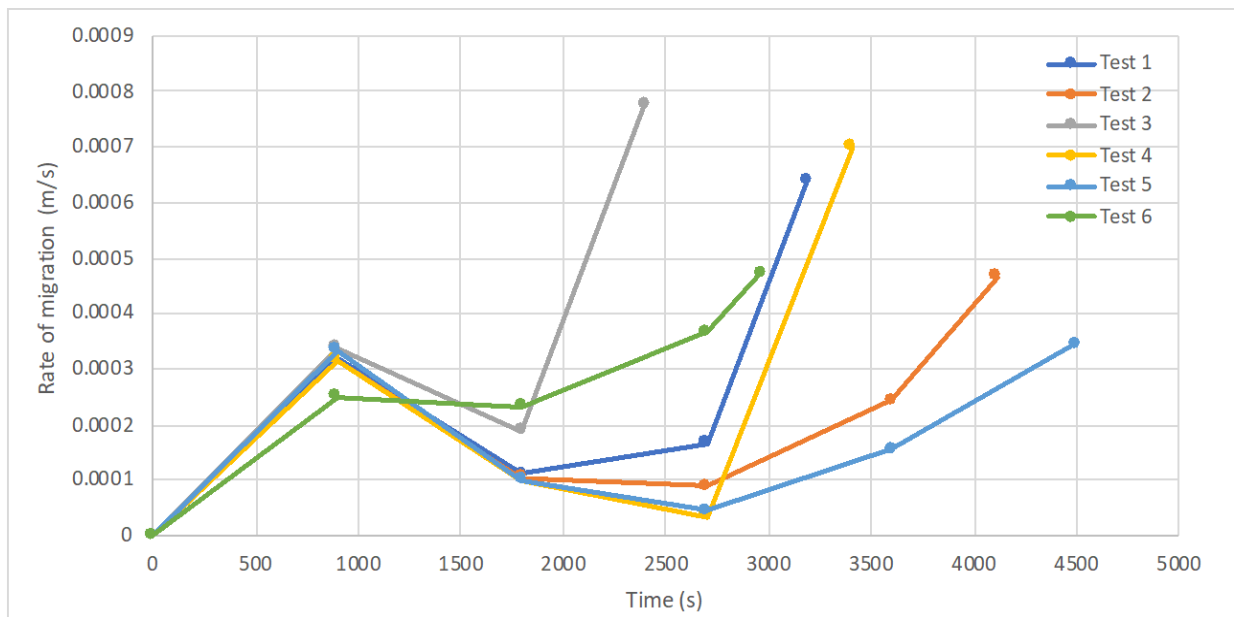

Figure 15: Scatter graph with lines of the migration rate data for the whole field against current. The results were taken from the aerial footage. There is a data point for each 15 minute period from the beginning of the test until the ripple field extends beyond the view of the camera. The last data point is when the view of the ripple field is lost.
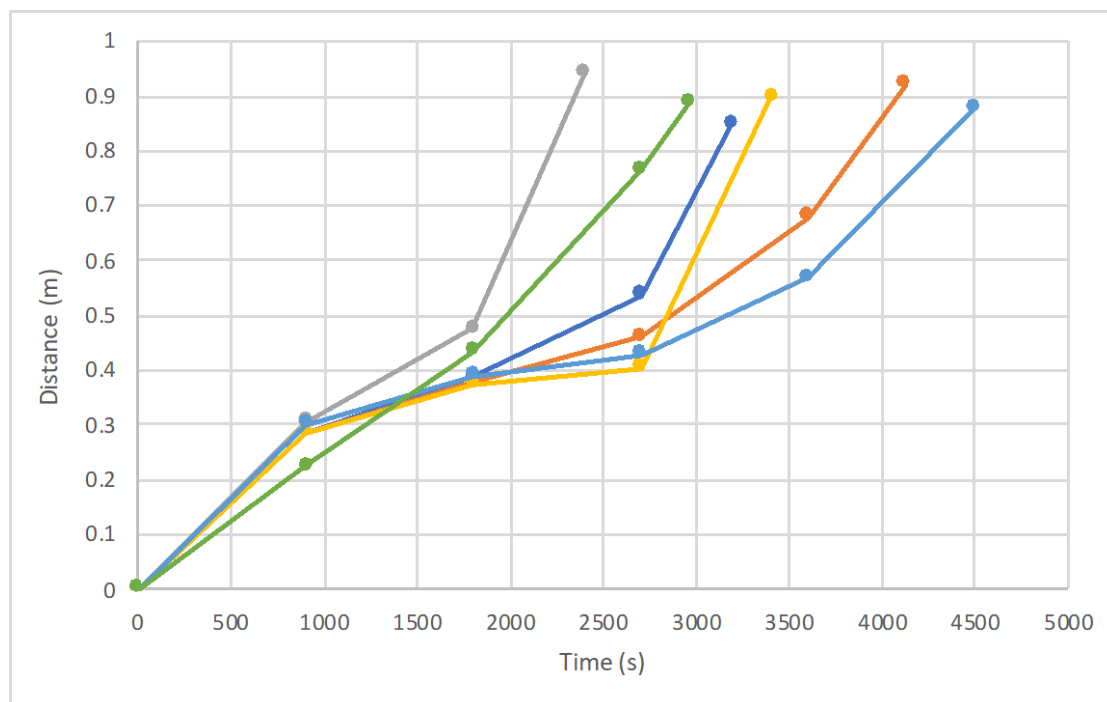
Figure 16: Scatter graph with lines of the distance data for the whole field against current. The results were taken from the aerial footage. There is a data point for each 15 minute period from the beginning of the test until the ripple field extends beyond the view of the camera. The last data point is when the view of the ripple field is lost. The same key has been used as Figure 25.

Figure 18 and Figure 19 are plotted from data taken from the videos every 15 minutes. Both plots suggest there are patterns in the data. Figure 18 shows the rate of migration is rapid initially and then reduces in each test, before increasing again before exiting the view of the camera. Figure 19 shows there is also a similar trend in the distance data. The distance of the front edge of the ripple field front, from the pile, increases with time; rapidly initially, then there is a more gradual increase before becoming rapid again.

The gradient of each line in Figure 19 is the migration rate of the ripple field, for that 15 minute period of the test. Unexpectedly, Test 1 did not yield the fastest migration rates. It was assumed that the highest current speed would obtain the greatest distance, however Test 3 grows the most rapidly. It can also be seen that despite very similar forcing conditions in Test 4 and Test 6, there is some spread in the response suggesting it is unlikely that the test is exactly repeatable.

Figure 18 may suggest that there is a peak in the migration rate of the ripple field front at 0.187 m/s, which could be due to this being an optimum speed for sediment movement in the tested conditions or suggest that, at faster current speeds there is more sediment movement from upstream so the ripples are filled in and the migration rate cannot be accurately calculated.

Individual Ripple Migration

Trends have been identified within the individual ripple migration data by plotting distance against time to give migration rate, and distance and migration rate against current.
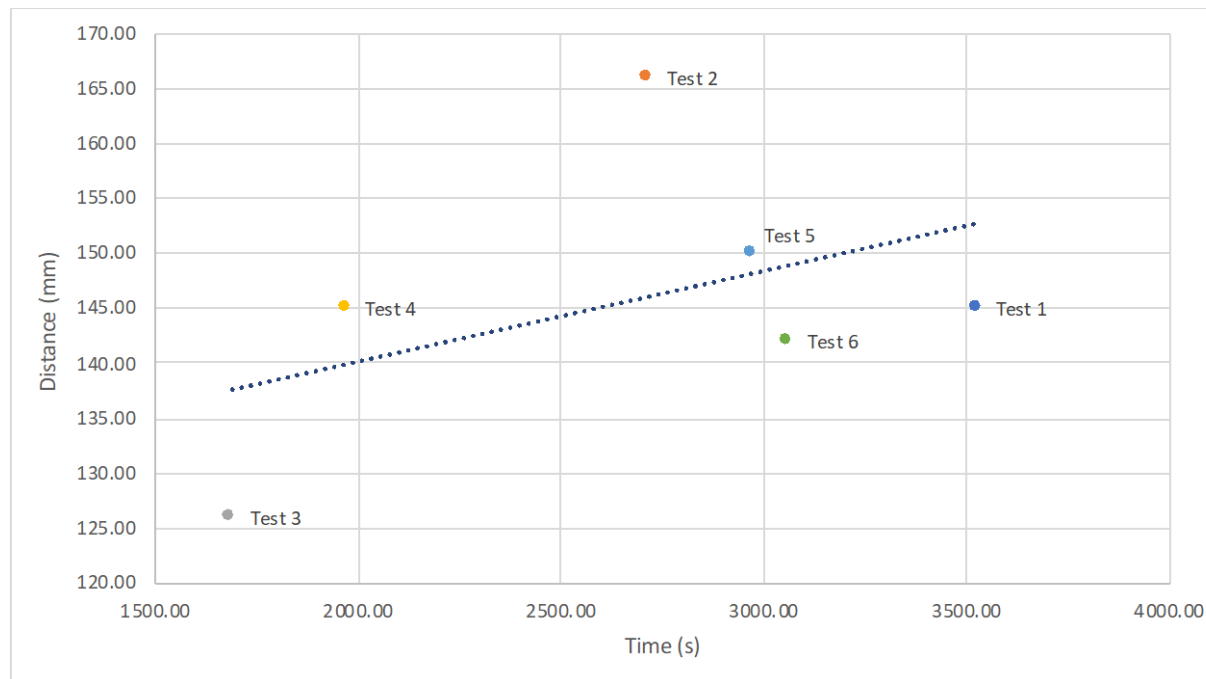

Figure 17: Plot of migration distance against time for the chosen individual ripples from each test.

As expected, the linear trendline on Figure 20 is the average rate of migration of the ripples and shows that the distance the individual ripples have travelled increases with time. The average rate of migration is 0.000058 m/s; the individual ripple fronts move considerably slower than the ripple field front.

The linear trendline on Figure 21 proposes that the rate of migration of the individual ripple fronts decreases with increasing current speed, whereas the linear trendline on Figure 17 suggests the ripple field front migration rate is almost constant. The trendlines suggest that increased current speed produces shorter individual ripples despite the ripple field front growing at the same rate.
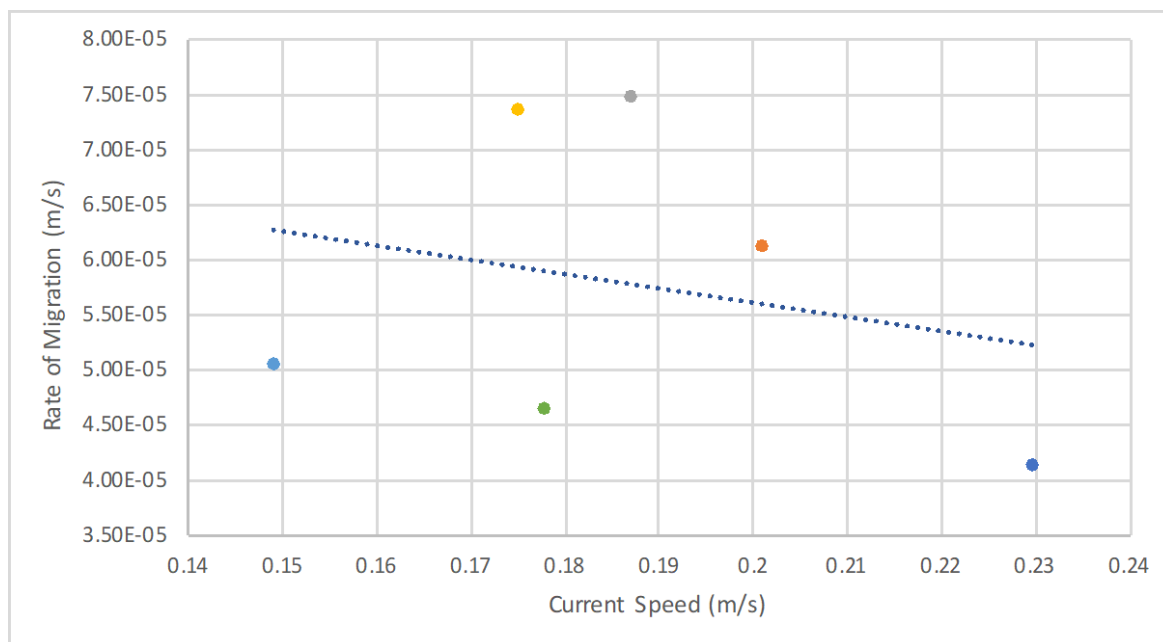
Figure 18: Graph of the rate of migration of the chosen individual ripple front, for each test, against the current speed.

This is partially corroborated by visual comparison of the footage; Figure 22 shows all 6 tests at the same test duration. It is clear that test 3 has the largest wavelengths and therefore follows that test 1 and 2 have smaller wavelengths, however it is not obvious visually if tests 4, 5 and 6 continue to follow the trend presented in Figure 17.
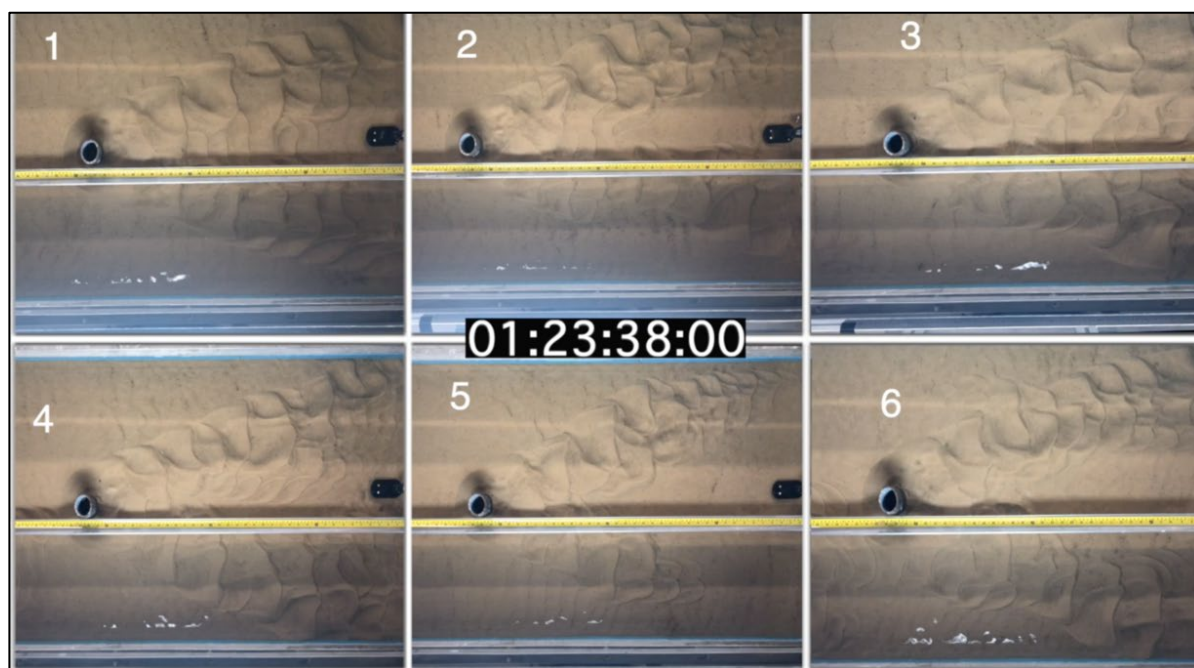

Figure 19: Screenshot of the compilation video showing the visual results of all 6 tests from the aerial camera. All tests had been run for 1 hour 23 minutes and 38 seconds.

To determine the relationship between the propagation rate of the ripple field front and the rate of the individual ripple from each test.

$$Ratio\ of\ rate\ of\ propagation\ = \frac{P_{RF}}{M_R}$$

Where P_{RF} is the propagation of the ripple field front and M_R is the migration rate of the individual ripples. The field propagates approximately 4 times faster than the individual ripple speed.

Figure 23 produces a linear trendline showing that the distance that the individual ripple fronts have travelled increases slightly with increasing current speed. As the distance travelled is a multiple of the wavelengths produced, this suggests that the wavelengths may not be purely based on the size of the grains as seen in $\lambda_r = 1000D_{50}$, however, there is considerable spread in the data, with tests 2 and 3 positioned far from the trendline.
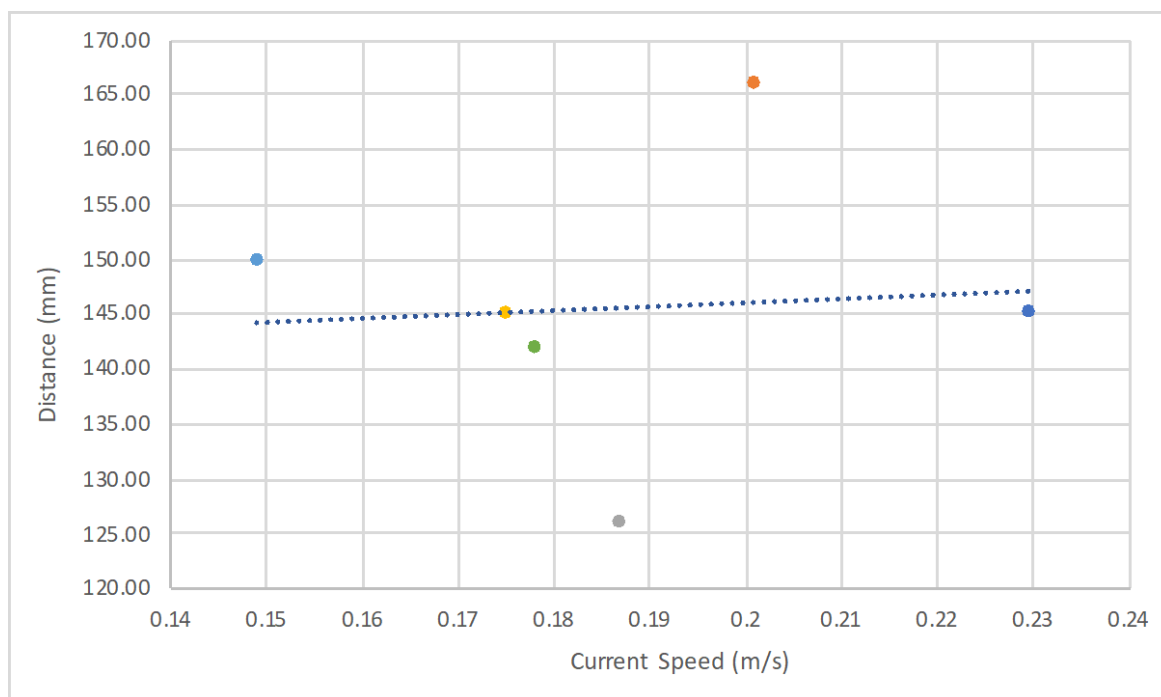

Figure 20: Graph of the distance travelled of the chosen individual ripple front, for each test, against the current speed.

Wavelength
As shown in Figure 22 there is some variation in the wavelengths across the 6 current speeds, however there is not an obvious pattern observed. According to $\lambda_r = 1000D_{50}$ the wavelength is only dependent on the diameter of the sediment, however the images show this may not necessarily be true and the self-organisation theory suggests that the wavelength will increase in a logarithmic manner forever if the conditions do not change.

Figure 24 shows 4 screenshots of the progress of Test 1. It can be seen that the shape of the ripples changes considerably throughout the time of the test and consequently the wavelengths also change. The last screenshot shows that the evolution of the ripples may begin as more representative linguoid shape, similar to semi-circles, then become the heart shape that has developed in the ripples closest to the scour pit.
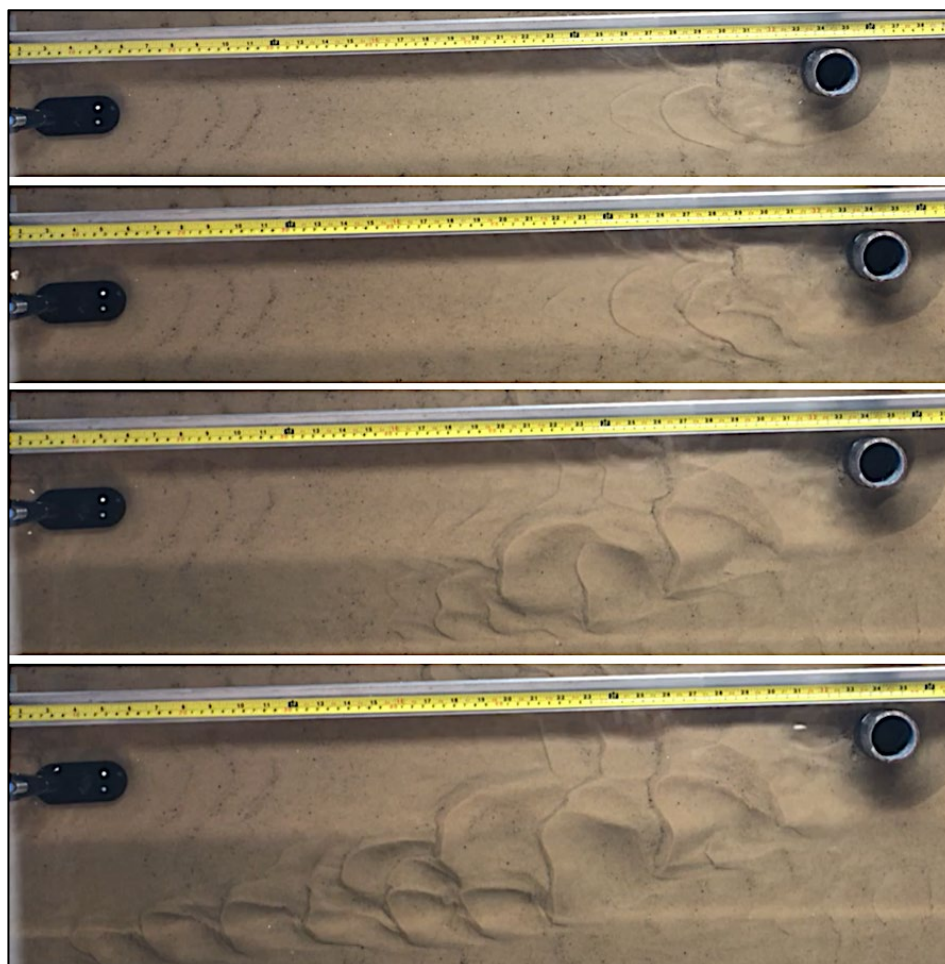

Figure 21: Screenshot of Test 1 progress at 15 minutes intervals then the last shot before the disturbance went beyond the camera view.

Ripple Height
It is likely that ripple height is the determining factor for the length of the ripple field. There are no reasons for the ripple field not to continue to propagate continually apart from the depth of each ripple reducing to zero, so a disturbance is no longer apparent. Figure 25 shows a cross-section down the centre of the rig for Test 2. Directly downstream of the pile the disturbance returns to the natural seabed formation quite quickly; returns to 0 mm at approximately 750 mm suggesting that the angle of the 2 sides of the wake is now too great for the disturbance to occur in the centre, or that as the disturbance has now reached 0 mm it will no longer propagate.
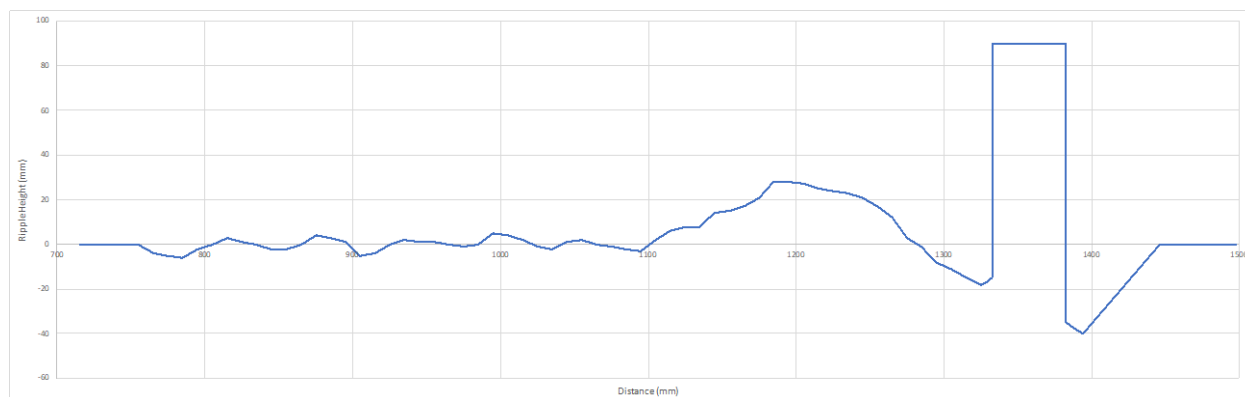
Figure 22: Plot of the length of the ripple field against the ripple height at the end of Test 2. The measurements were taken as a centre cross-section of the pile.

If the scour wake is the area of disturbance beyond the scour pit then the wake in Figure 25 is 530 mm long, which is equivalent to 10.6 pile diameters. Figure 26 shows the centreline cross-section plot for Test 3.
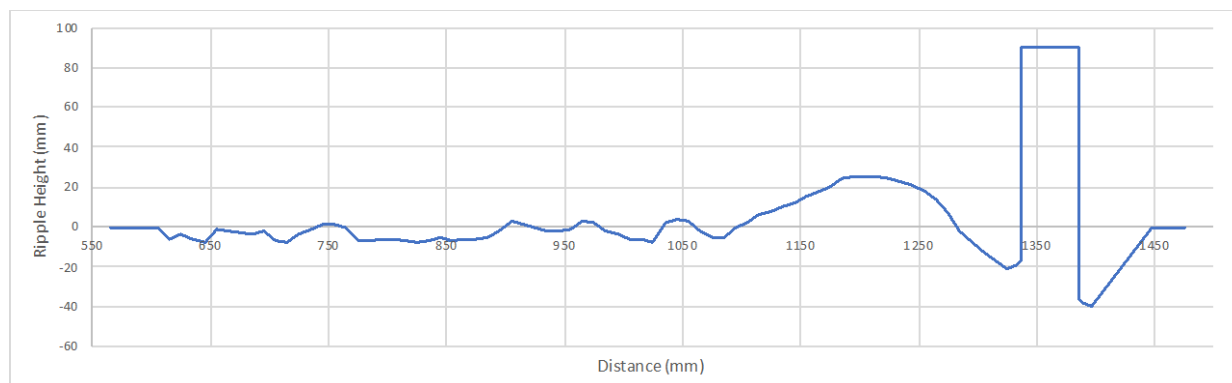

Figure 23: Plot of the length of the ripple field against the ripple height at the end of Test 3. The measurements were taken as a centre cross-section of the pile.

The wake in Figure 26 is 675 mm long, which is equivalent to 13.5 pile diameters. Figure 27 shows the centreline cross-section plot for Test 5.
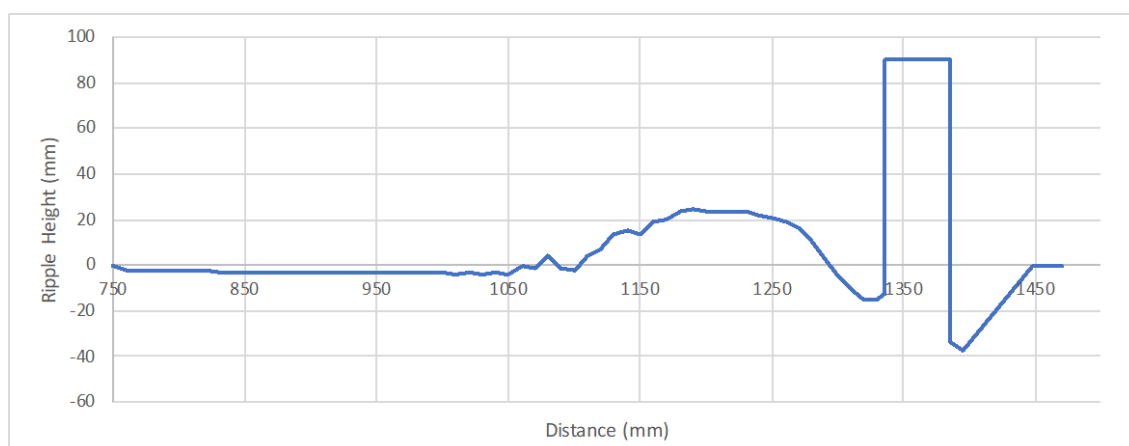

Figure 24: Plot of the length of the ripple field against the ripple height at the end of Test 5. The measurements were taken as a centre cross-section of the pile.

The wake in Figure 27 is 545 mm long, which is equivalent to 10.9 pile diameters. There is no pattern formed by the 3 cross-section observations but there are significant differences in how the plots look. Figure 27 is significantly different to the previous 2 cross-sections as it has a large mound, as seen in the other observations, but then a long continuous depression rather than multiple individual ripples.

Angle of propagation
The angle of propagation appears to be similar for each test in the visual comparisons. Figure 28 shows the method used to determine the angle of propagation from Test 4; approximately 17°.

Figure 25: Sketch to determine the angle of propagation of the scour wake from Test 4

By completing the same analysis for all of the tests the following results are produced in Table 8.

Table 8: Angle of propagation for each test

Test	Current Velocity (m/s)	Angle of propagation (°)
1	0.230	16.5
2	0.201	20.9
3	0.187	19.3
4	0.175	16.6
5	0.149	24.1
6	0.178	18.2

From visual comparison, in Test 6 it would appear that the angle reduces far downstream from the pile, however this is believed to be due to the influence of the

sides of the rig; an affect that would not be present in reality as offshore wind farms are typically placed far enough offshore to not be interrupted by other structures.

Discussion

Variability and Spread

Each experiment produced random results with large variability across all 6 tests. If the testing process was repeated, using the same forcing conditions, then it is likely the results would be different. This is corroborated by the data from Test 6 as this did not produce significantly similar results to Test 4. Instead, the results from Test 1 were almost identical to Test 4 proving the variability in the reaction of sediment to the experimental conditions. Miles and Thorpe (2015) also found significant spread and large variability in their study; data observed that even with the same mean flow strength there were multiple different responses, providing evidence for confidence in the reported experiment.

Despite the variability and spread there were a number of trends apparent in all 6 tests: acute angle of propagation; linguoid ripple formation; migration rate of the ripple field front being significantly faster than the individual fronts.

Migration Rate

It has been determined that the bedform disturbance propagates significantly faster than the individual ripple speed; approximately 4 times faster. This may suggest that more ripples are developing faster than the existing ripples are growing, and the new ripples are becoming the front of the ripple field.

The ripples also develop laterally, however this was not known to have occurred before the testing began so unfortunately there was no measuring equipment suspended across the width of the rig; further work may benefit from measuring the lateral migration rate too.

Wavelength and ripple height

The visual comparisons of the footage across all of the tests, and the closer look into Test 1, suggest that the wavelengths of the ripples are not only dictated by the size of the sediment as they appear to grow and develop throughout the testing. These visual observations begin to suggest that the wavelengths may develop as described by Gallagher (2011) in the self-organisation theory. Figure 29 and Figure 30 show the method used to determine the wavelengths and ripple heights for Test 4. The horizontal coloured lines represent the start and end of the individual ripples while the arrows mark the peaks and troughs of the ripples.
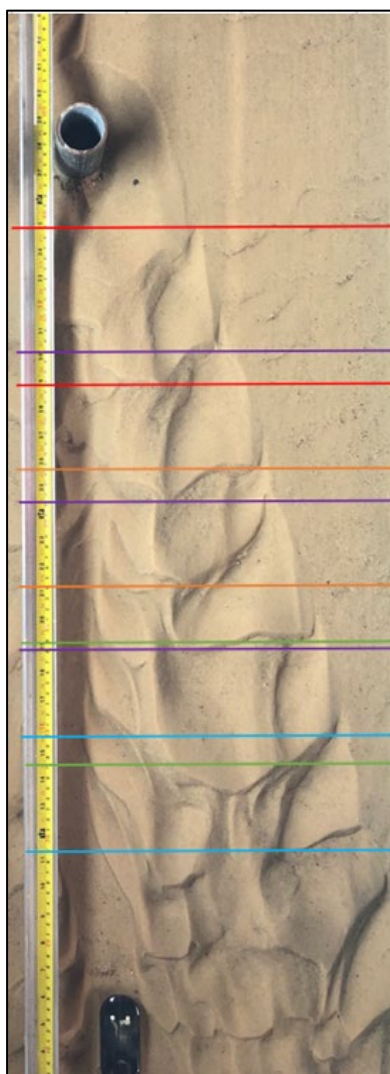
Figure 26: Identifying the beginning and end of each ripple - crest to crest
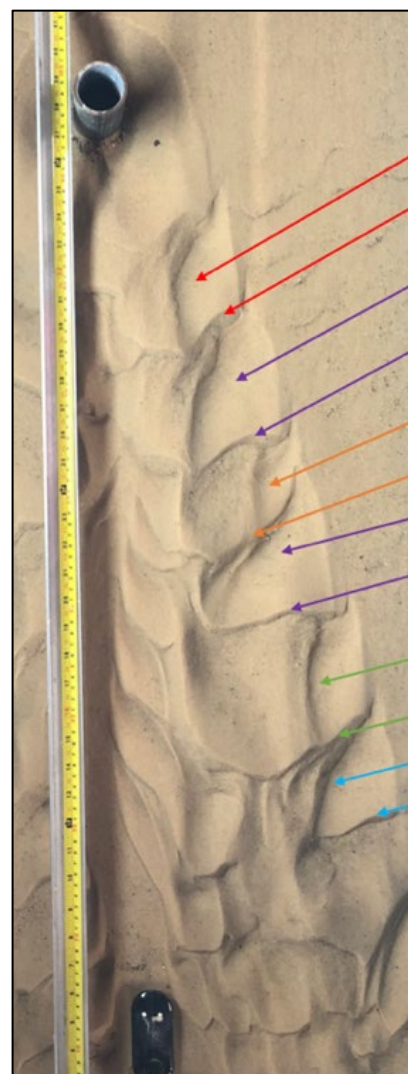
Figure 27: Identifying the peaks and troughs of the ripples

The colours shown in the above figures directly relate to the colours in Table 9 and the values have been determined by reading the measurements from the tape and subtracting the downstream value from the upstream value. The ripple index is the ratio between the wavelength and the wave height.

Table 9: Observed wavelength, wave height and ripple index for data for Test 4. Calculated wavelength and wave height using the observed wavelength, d_{50}=0.2 mm and given equations to allow comparison between calculated and observed values.

	Observed Wavelength (mm)	Calculated Wavelength (mm)	Observed Wave Height (mm)	Calculated Wave Height (mm)	Ripple Index
🟥	162	200	20	23.14	8.10
🟪	153	200	22	21.86	6.95
🟪	149	200	22	21.29	6.77
🟧	110	200	16	15.71	6.88
🟩	119	200	17	17	7.00
🟦	118	200	20	16.86	5.90

The index for ripples in unidirectional flow is between 8 and 15. As the experiment was completed in unidirectional current flow it would be assumed that all the ripple index values should be between these parameters, however as seen in Table 9 only 1 ripple index value fits this category. The remaining values all fit into the category of vortex ripples in oscillatory flow (Masselink and Hughes, 2003) which could suggest that the wavelengths had not reached the expected magnitude and consequently the ratio between the wavelength and height was too small. It may also suggest that the ripple heights were too high and had not yet stabilised to the correct value. Additionally, the inaccuracies of the data matching that described by Masselink and Hughes (2003) could suggest that the flow did in fact have some minor oscillations present to have caused the ripple index values to be smaller than expected, such as reflections from the end boundaries of the rig or the adjustable paddle.

Limitations and errors
As the majority of the results have been gathered from videos, rather than in real time during the experiment there are additional errors that may have influenced them. The resolution of the crests in each video is approximately +/- 3mm. Additionally, the time is visible on each recording in hh:mm:ss therefore the error in accuracy is +/- 1s. The overall accuracy of the rate of migration is +/- 1.5% of the calculated result.

The experiment detailed in this report considered only 1 pile with relatively small diameter which was chosen due to the scale of the equipment available. Although the chosen pile diameter was small, it is similar to Petersen et al (2015) who found his results mimicked those with larger piles. Petersen et al (2015) tested pile diameters of 50, 70, 75 and 100 mm. Additionally, the Scroby Sands windfarm site has monopiles with a diameter of 4.2 m (Whitehouse et al, 2011) which would be represented by a model pile of 42mm; smaller than the tested model pile diameter of 50mm.

Reeve, Chadwick, Fleming (2018) state, based on fieldwork at Teignmouth and Egmond, that the inaccuracy of an electro-magnetic flow meter is a maximum of approximately 15% for velocities that are time-averaged greater than 0.5 m/s. All current speeds measured in the testing were greater than this, however this 15% error could be apparent. The data sheet (Valeport, 2019) states the accuracy of the device used is +/- 0.5% of the reading plus 5 mm/s. Future testing may use an impellor too to corroborate the results of the flow meter.

Only unidirectional current flow was modelled, however Petersen et al (2015) found that current is the element of flow that yields the largest scour depth in the area downstream of the pile and therefore the governing flow for scour wake.

Lighting
During the setup of the equipment it became apparent that the lighting above the rig was going to cause significant shadows, making it challenging to distinguish the peaks and troughs of the ripples from the videos. To minimise the shadow effects, the lighting above the rig was covered and an LED panel light was set up on the side of the rig. The LED panel was positioned at an angle to minimise the shadows that this caused. It was positioned parallel to the camera to ensure there was significant

lighting in the filmed area. In future work it may be beneficial to have lighting also at the end of the tank to help distinguish between peaks and troughs in the video.

Level of tank

Unfortunately, it became apparent throughout the testing that the water level was not consistent throughout the tank, attributed to the rig not being level in all planes. There is potential that this may have affected the results, but it is assumed this will be minimal as the maximum difference in depth was approximately 5 mm.

Depth vs. Speed
When determining the depth of water to be used in the experiment, considerations had to be made for the flow speed. The current speed could be increased with a shallower water depth; balance had to be met between the two variables. The depth had to be great enough to be realistic however, the speed had to be great enough to ensure the sediment transport to create ripples. The speed, therefore, had to be greater than the threshold velocity for the sediment.

Further Work
There is reason to believe that future work would be beneficial to establish the affect that waves and current, together, have on the propagation of the scour wake. It may be valuable to complete a larger scale experiment to corroborate the results collected in this report and reduce the influence of the rig on the response of the sediment.

Further work could benefit from the use of an autonomous sand ripple profiler which could enable the whole sediment bed profile to be recorded at the end of each experiment. The profiler could also be used throughout the testing, however it is likely the flow of water would have to be stopped to enable the profiler to obtain accurate results. If the flow was stopped every half an hour, for example, to obtain a profile then the experiment could yield unrealistic results due to the flow being stopped and restarted. Reeve, Chadwick and Fleming (2018) completed fieldwork using an autonomous sand ripple profiler at Egmond where profiles were measured every few minutes and at Spratt Sands, Teignmouth, where the bed features are very prominent.

The scour wake may also be influenced by tide so further work may go some way to try to establish how the tidal pattern will affect the path of the wake

Applicability of Results
Ripple fields are incredibly important for cable runs and these results suggest that the pile effects a much greater area than just the scour pit. The work established within this report suggests that designs need to consider the effects of scour for a much more substantial distance, potentially the effects of the previous monopile on the next. The effects of one pile on the next has previously been seen at Scroby Sands where the scour wake extends from the originating monopile to its nearest downstream neighbour (Rees, 2006), with a typical volume of change of sediment of 10000 – 25000 m^3. The smallest distance between the monopiles at Scroby Sands is 320 m suggesting that the scour wake has extended this distance. These values

show there has been a vast impact observed on the seabed, caused by the disturbance to flow produced by the monopiles.

Table 10 shows the scaled-up distance affected in the prototype for each test after 5 hours. The distances have been scaled up from the distance travelled by the whole ripple field in 30 minutes of model time.

Table 10: Scaled up prototype distances

Test	Current Speed (m/s)	Time (hh:mm:ss)	Distance (mm)	Distance (m)
1	0.23	05:00:00	40000	40
2	0.201	05:00:00	39500	39.5
3	0.187	05:00:00	48500	48.50
4	0.175	05:00:00	39000	39
5	0.149	05:00:00	39200	39.20
6	0.178	05:00:00	45500	45.50

In just 5 hours, within 1 tide, there is potential for the scour wake to have affected over 40 m straight line downstream distance from the monopile. It is likely that the tide and wave conditions could increase this even further. As the wake propagates at an angle a very large area is being affected by this downstream distance.

If it is assumed from (Rees, 2006) data that the minimum typical volume change of 10000 m^3 relates to the smallest distance between piles (320 m) then there is 31.25 m^3 of change per m. This means that in just 5 hours there is approximately 1250 m^3 of volume change.

Conclusion
The aim of the research was to begin to understand the propagation of scour wake downstream of monopiles due to the dramatic impacts it can have on the cable runs between the structures, when used for windfarms. The research has produced varied results due to the unpredictability of sediment movement, but with obvious trends found across the data. It was observed in every test that the scour wake forms in 2 distinct lines, each propagating at an angle of approximately 20° from the direction of flow. As the experiment was completed in unidirectional current-only flow it is likely that this would be different in the field due to the impact of waves and tides.

It was also observed, consistently, that the migration of the ripple field front is 4 times faster than that of the individual ripples in the disturbance. The data was analysed according to the aerial projection footage taken for the duration of each test.

Each of the disturbances presented themselves as linguoid ripples, however there were some discrepancies on whether they were created by unidirectional flow or oscillatory flow due to the ripple index calculated. As the test was completed with unidirectional flow, only, it would suggest that there may have been some reflection present within the rig to create the vortex ripples.

The limitations of the equipment used presented some small model effects and therefore the research would benefit from further work into the propagation of the

ripples using a larger facility and a more accurate method of measurement such as an automated ripple profiler.

The report goes some way into understanding the evolution and propagation of the scour wake downstream from the monopiles. It shows that a significant area can be impacted by the disturbance of the scour wake due to a large volume of sediment being transported. The disturbances can span between the monopiles, so it is essential more consideration is given to the scour wake, rather than just the scour pit, during the design of offshore structures.

References

4Coffshore. (2013) *Monopile Foundation*. Available at: https://www.4coffshore.com/windfarms/monopiles-support-structures-aid4.html (Accessed/downloaded: 5th December 2018).

4Coffshore. (2013) *Monopile Support Structures*. Available at: https://www.4coffshore.com/windfarms/monopiles-support-structures-aid4.html (Accessed: 5th December 2018).

Carter, J.M.F. (2007) 'North Hoyle offshore wind farm: design and build', *Energy 160*, EN 1 , pp.21-29.

CIRIA (2007). *The Rock Manual. The use of rock in hydraulic engineering (2nd edition)* London: CIRIA

CIRIA (2015) *Manual on scour at bridges and other hydraulic structures.* 2nd edn. London: CIRIA.

Clarke, L.B., and Werner, B.T. (2004) 'Tidally modulated occurrence of megaripples in a saturated surf zone'. *Journal of Geophysical Research.* 109 (C01012) doi: 10.1029/2003JC001934.

Department of Energy and Climate Change (2008) 'Dynamics of scour pits and scour protection – Synthesis report and recommendations.'

Firth, K. (2019) *Investigating the evolution of sedimentary features near monopoles*. 30 April. Available at: https://www.youtube.com/watch?v=k8oxVOpo74g&feature=youtu.be (Accessed: 1 May 2019).

Gallagher, E.L. (2011) 'Computer simulations of self-organized megaripples in the nearshore.' *Journal of Geophysical Research.* 116(F01004) doi: 10.1029/2009JF001473

HR Wallingford (2017). *Learning to assess marine scour risk*. Available at: http://www.hrwallingford.com/news/learning-to-assess-marine-scour-risk [Accessed 5 Dec. 2018].

Leeder, M.R. (1982) *Sedimentology - Process and Product*. London: George Allen & Unwin (Publishers) Ltd.

Li, Q., Prendergast, L.J., Askarinejad, A., and Gavin, K. (2018) 'Effect of scour on the behaviour of a combined loaded monopile in sand'

Masselink, G. (2019) *Coastal impacts of extreme storms in a changing climate.* [Public Lecture]. University of Plymouth. 23 Jan.

Masselink, G., and Hughes, M.G. (2003) *Introduction to Coastal Processes & Geomorphology.* London: Hodder Arnold.

Miles, J. (2018) Conversation with Kate Firth, 11th October.

Miles, J., Martin, T. and Goddard, L. (2017). *Flow processes near wind farm monopoly foundations*. [image] Available at: https://www.sciencedirect.com/science/article/pii/S0378383917300054 [Accessed 5 Dec. 2018].

Miles, J., and Thorpe, A. (2015) 'Bedform contributions to cross-shore sediment transport on a dissipative beach.' *Coastal Engineering,* 98, pp. 65-77.

Navionics (2019). 'Gunfleet Sands' Available at: https://webapp.navionics.com/?lang=en#boating@9&key=iq%7CzHswhF [Accessed: 20 Apr. 2019].

Petersen, T.U., Sumer, B.M., Fresoe, J., Raaijmakers, T.C., Schouten, J.J. (2015) 'Edge scour at scour protections around piles in the marine environment – Laboratory and field investigation.' *Coastal Engineering*, 106, pp.42-72.

Pye, K. (1994). *Sediment transport and depositional processes*. Oxford: Blackwell Scientific Publications.

Rees, J. (2006). 'Scroby Sands Offshore Wind Farm – Coastal Processes' Monitoring. *CEFAS.*

Reeve, D., Chadwick, A., and Fleming, C. (2018) *Coastal Engineering - Processes, Theory and Design Practice*. Boca Raton: CRC Press.

RenewableUK. (n.d.) *Wind Energy – RenewableUK.* [online] Available at: https://www.renewableuk.com/page/WindEnergy [Accessed 15 Apr. 2019]

Sørensen, J. D. and Sørensen J.N. (2010) *Wind Energy Systems: Optimising Design and Construction for Safe and Reliable Operation*, Elservier.

Soulsby, R. (1997) *Dynamics of marine sands. A manual for practical applications*. London: Thomas Telford Publications.

Sumer, B.M., Christiansen, N. and Fredsoe, J. (1992). 'Time scale of scour around a vertical pile.' *Port, Coastal and Ocean Engineering.,* 119(5).

Thies, P.R., Johanning, L., and Smith, G.H. (2012). 'Assessing mechanical loading regimes and fatigue life of marine power cables in marine energy applications.' *Proceedings of the Institution of Mechanical Engineers, Part O: Journal of Risk and Reliability*

Valeport. (2019) *Model 801 Electromagnetic Flow Meter.* [online] Available at: http://www.valeport.co.uk/Portals/0/Docs/Datasheets/Valeport-Model-801.pdf [Accessed 22 Mar. 2019]

Werner, B. T. (1999), Complexity in natural landform patterns, Science, 284, 102–104.

Whitehouse et al. (2011) 'The nature of scour development and scour protection at offshore windfarm foundations.' *Marine Pollution Bulletin*, 62(1), pp.73-88.

Whitehouse, R. (1998) *Scour at marine structures*. London: Thomas Telford Publications.

Whitehouse, R.J.S., Harris, J.M., Sutherland, J., Rees, J. (2011) 'The nature of scour development and scour protection at offshore wind farm foundations', *Marine Pollution Bulletin*, 62, pp.73-88.

WindEurope. (2019) *Offshore Wind in Europe.* [online] Available at: https://windeurope.org/wp-content/uploads/files/about-wind/statistics/WindEurope-Annual-Offshore-Statistics-2018.pdf [Accessed 15 Apr. 2019]

Zanke, U.C.E., Hsu, T., Roland, A., Link, O., and Diab, R. (2011) 'Equilibrium scour depths around piles in noncohesive sediments under currents and waves', *Coastal Engineering,* 58, pp. 986-991.